Oblique-incidence illumination and collection for depth-selective fluorescence spectroscopy

T. Joshua Pfefer
Anant Agrawal
Food and Drug Administration FDA/CDRH/HFZ-130
Center for Devices and Radiological Health
12725 Twinbrook Parkway
Rockville, Maryland 20852
E-mail: joshua.pfefer@fda.hhs.gov

Rebekah A. Drezek
Rice University
Department of Bioengineering
Houston, Texas 77251

Abstract. Optimization of device-tissue interface parameters may lead to an improvement in the efficacy of fluorescence spectroscopy for minimally invasive disease detection. Although illumination-collection geometry has been shown to have a strong influence on the spatial origin of detected fluorescence, devices that deliver and/or collect light at oblique incidence are not well understood. Simulations are performed using a Monte Carlo model of light propagation in homogeneous tissue to characterize general trends in the intensity and spatial origin of fluorescence detected by angled geometries. Specifically, the influence of illumination angle, collection angle, and illumination-collection spot separation distance are investigated for low and high attenuation tissue cases. Results indicate that oblique-incidence geometries have the potential to enhance the selective interrogation of superficial or subsurface fluorophores at user-selectable depths up to about 0.5 mm. Detected fluorescence intensity is shown to increase significantly with illumination and collection angle. Improved selectivity and signal intensity over normal-incidence geometries result from the overlap of illumination and collection cones within the tissue. Cases involving highly attenuating tissue produce a moderate reduction in the depth of signal origin. While Monte Carlo modeling indicates that oblique-incidence designs can facilitate depth-selective fluorescence spectroscopy, optimization of device performance will require application-specific consideration of optical and biological parameters. © *2005 Society of Photo-Optical Instrumentation Engineers.* [DOI: 10.1117/1.1989308]

Keywords: fiber optics; fluorescence spectroscopy; Monte Carlo modeling.

Paper 04148RR received Aug. 3, 2004; revised manuscript received Mar. 8, 2005; accepted for publication Mar. 14, 2005; published online Aug. 1, 2005.

1 Introduction

The field of optical diagnostics has the potential to improve public health by providing rapid, minimally invasive disease detection with greater accuracy and less cost than current standards of care. One of the most promising approaches in this area is UV-VIS fluorescence spectroscopy, which has been demonstrated to be highly effective for a variety of applications including neoplasia detection.[1] While this technology is approaching clinical viability, it is likely that further developments may enhance diagnostic efficacy. Research on excitation and emission wavelengths and discrimination algorithms has elucidated issues relevant to system optimization. However, in spite of the myriad of fiber optic probe designs that have been implemented in prior studies,[2] the literature provides little information about the influence of device-tissue interface design on diagnostic efficacy or parameters that may influence disease diagnosis, such as signal origin and intensity.

In recent years, there has been rising interest in the role of device-tissue interface parameters. Studies on normal-incidence illumination-collection schemes have indicated that parameters such as fiber diameter, source-detector separation, and probe-tissue spacing strongly affect relative sensitivity to fluorophores in turbid media.[3–7] These variations in spatial sensitivity have the potential to be exploited *in vivo* for targeting of specific tissue layers that are most diagnostically relevant, as suggested previously.[8,9]

Several prior studies of fiber optic probe design for Raman spectroscopy have investigated the use of fibers that are beveled to induce an optical deflection, such that excitation light enters the tissue at a non-normal angle to the surface.[10–12] Similarly, beveled tip collection fibers detect light exiting tissue at an angle. For media with low turbidity, the location where illumination and collection cones overlap is interrogated in a highly selective manner. A simple illustration of this effect is shown in Fig. 1. The top row of diagrams indicates how angled overlapping spot (e.g., single-fiber) probe geometries cause an increase in selectivity to the most superficial regions, whereas the second row indicates how angled nonoverlapping spot geometries could maximize selectivity to

Address all correspondence to T. Joshua Pfefer, Center for Devices and Radiological Health, Food and Drug Administration, FDA/CDRH/HFZ-130 — 12725 Twinbrook Parkway, Rockville, MD 20852.
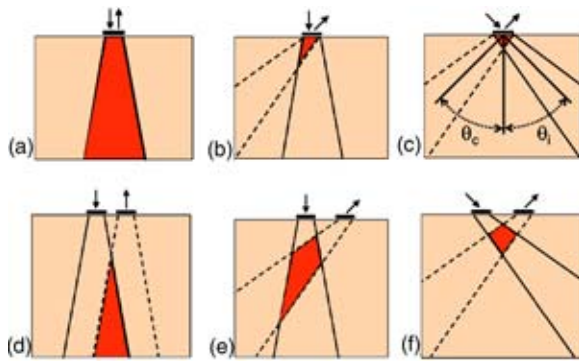
Fig. 1 Illustration of illumination (solid lines) and collection (dashed lines) cones for normal- and oblique-incidence geometries. Darkened areas indicate the regions of overlap, and thus maximum sensitivity. Diagram in (c) indicates how illumination (θ_i) and collection (θ_c) angles were defined.

subsurface regions. These cases illustrate the basis of oblique geometry selectivity; however, scattering and absorption cause changes in the location and shape of the targeted region. It must also be noted that while Figs. 1(a)–1(c) contain probe designs that are not realistic representations of true single-fiber angled probes, overlapping illumination and collection spots might be achieved through noncontact multifiber probes or free beam approaches.

A prior investigation of angled fiber optic probe designs for fluorescence spectroscopy in epithelial tissue[13] presented computational and *in vivo* results on the behavior of angled interface geometries. This study found that when an angled illumination fiber was used, the variations in relative sensitivity to epithelial and stromal layers obtained by changing illumination angle and fiber separation distance provided control over relative selectivity that was superior to that obtained using normal-incidence probes. Additionally, a recent study demonstrated the efficacy of an angled fiber approach to reflectance spectroscopy.[14] While these results provide an initial proof of principle for a novel approach to optimizing depth-resolved selectivity of tissue fluorophores, and strong insights for a specific layered tissue geometry, numerous unresolved issues remain regarding the underlying light propagation mechanisms, variations in signal origin, and approaches for device optimization.

In this study, we perform a parametric computational investigation of the effect of a device-tissue interface with angled delivery and collection. The goals of this project were to characterize general trends in selectivity and signal intensity due to device parameters and optical properties, and to distill salient information on light-tissue interaction and device optimization from this data. Specifically, we have implemented a Monte Carlo model to simulate how variations in the illumination and collection angle, spot separation distance, and tissue optical properties influence the origin and intensity of detected fluorescence signals.

2 Methods

Simulations were performed using a Monte Carlo model of fluorescence spectroscopy nearly identical to those used in our prior studies.[3,4] The major differences in the new model are:

1. variable angle of illumination and collection (θ_i and θ_c, respectively, where both angles are defined with respect to normal incidence); 2. multiple collection geometries were specified for each delivery scheme; and 3. the detector was simulated as a single circular spot rather than a concentric ring (due to a lack of symmetry in many cases).

Given that a wide variety of device designs may be used to achieve an oblique-incidence probe interface (e.g., fibers in air or direct tissue contact, lenses, mirrors, cones, etc.), our intent was not to investigate the performance of a specific approach, but to investigate general light-tissue interactions for oblique-incidence geometries. Therefore, relatively simple illumination-collection geometries were implemented based on approaches from prior studies.[3,4,12] Fiber numerical aperture was assumed to be 0.22. For each of the two oblique angles investigated, the illumination and collection cones were defined by a pair of angles relative to the normal to the tissue surface. The shallow angle case was defined by the angle pair 12.6/31.6 deg and is referred to by its average angle, 22 deg. The sharper angle case was defined by the angle pair 35.0/55.3 deg and is referred to by its average angle, 45 deg. Photons were launched in a uniform spatial distribution over a circular spot and in a uniform angular distribution through the specified cone angle. Simulations were performed with illumination and collection spots either in an overlapping geometry or with edge-to-edge separation distances (L) of 0.025, 0.05, 0.1, 0.2, 0.4, or 0.75 mm.

Each photon absorbed in the tissue was converted to a fluorescence photon and propagated until absorbed or detected. Two assumptions are inherent in this simplified approach to the excitation-to-emission conversion process: 1. all absorption is due to a single fluorophore, and 2. the fluorophore has a quantum yield of 1.0. Therefore, signal intensities presented in the results show accurate trends but are not physically realistic in terms of absolute values. An important benefit of this approach is that it facilitates the calculation of realistic values for a wide range of situations through a simple multiplication of the simulated detected intensity by the fraction of total absorption due to the fluorophore (μ_{a_fl}/μ_{a_total}) and the fluorophore quantum yield.

A homogeneous tissue region $5 \times 5 \times 4$ mm (length $\times$ width $\times$ depth) was simulated. Since the probability of detecting photons that reached the edge of this region was minimal, such photons were terminated. Detected fluorescence photons were binned according to their emission location in a 2-D Cartesian matrix ($G[i,j]$), in which i and j correspond to the lateral and depth index of square bins measuring 0.025 mm on each side, and where i is defined to be in the plane that bisects the illumination-collection spots (as seen in Fig. 1). This approach effectively provides integration of all fluorescence events over the out-of-plane dimension. The resulting fluorescence origin distribution describes device sensitivity as a function of location within the tissue. Depth-wise emission distributions were calculated by summing $G[i,j]$ over all i, then normalizing the distribution to the total number of detected fluorescence photons.

The two sets of optical properties investigated are listed in Table 1. These cases were chosen to provide biologically relevant absorption (μ_a) and scattering (μ_s) coefficients at two distinct attenuation levels. The entire superficial surface was

Table 1 Tissue optical property cases.

Optical property case	Source	Wavelength	μ_a (mm^{-1})	μ_s (mm^{-1})	g	μ_s' (mm^{-1})
Low attenuation	Ref. 6 Ref. 8	460 nm	0.24	9.4	0.94	0.56
		520 nm	0.18	8.0	0.94	0.48
High attenuation	Ref. 9 Ref. 3	337 nm	1.3	20	0.9	2.00
		450 nm	0.4	10	0.9	1.00

assumed to have a refractive index of 1.45, which simulates a large probe that covers the tissue. The lateral and deep boundaries were index matched with the tissue at 1.37. One billion photons were used in each simulation to maximize distribution convergence for low collection efficiency cases while maintaining a marginally reasonable computation time of approximately 110 h on a 2.2-GHz dual-processor workstation (Dell Incorporated, Round Rock, Texas).

3 Results

Computational modeling results describing the effect of angled illumination-collection design on the intensity and origin of detected fluorescence are presented here. In all simulations performed, the geometry included one illumination and one collection spot, each having a diameter of 0.2 mm. For data presented in Fig. 2, the illumination and collection spots overlapped completely. The remainder of the data presented here (Figs. 3–7) involves nonoverlapping cases with edge-to-edge spot separation distances (L) from 0.025 to 0.75 mm.

Results for the overlapping spot cases are seen in Fig. 2. A design similar to the single fiber probes in our prior studies ($\theta_i = \theta_c = 0$ deg)[3,4] is represented with filled triangles. Changing θ_i or θ_c caused an increase in sensitivity to regions in the most superficial 50 to 100 μm. It is also worth noting that slightly greater selectivity—the ability to detect signals exclusively from a specific region—was achieved for $\theta_i = 0$ deg and $\theta_c = 45$ deg in comparison to the $\theta_i = 45$ deg and $\theta_c = 0$ deg geometry. This is seen as an increase in sensitivity for the very superficial regions and a corresponding decrease in deeper regions, and is likely due to differences in optical properties at the excitation and emission wavelengths, as well as differences in acceptance angle for the two detection geometries. Increasing attenuation caused an increase in selectivity to the superficial region, an effect that was most significant for the $\theta_i = \theta_c = 0$ deg case. Most of these effects are explained by the diagrams in Figs. 1(a)–1(c), which illustrate that the normal incidence case tends to collect fluorescence originating from a range of depths, yet when light is delivered or collected at an oblique angle, the cone overlap volume shrinks to a region close to the surface. 2-D plots are not provided in Fig. 3 for the overlapping probe geometry, because signal origin is limited to a very small region directly below the overlapping region and such graphs would not provide significant additional information than what is available in Fig. 2.

Spatially resolved fluorescence origin data are presented in Fig. 3 for the low attenuation case where the illumination-

collection spot separation distance (L) is 0.1 mm (edge-to-edge distance). For the $\theta_i = \theta_c = 0$ deg geometry [Fig. 3(a)], detected photons originated over a large region from the tissue surface to 1.0 mm deep. This detection region resembles the crescent shape typical of light propagation in tissue. A significant amount of noise is seen in this graph due to the relatively low total signal and the fact that detected photons originated from a wide range of positions. Increasing θ_c to 22 deg [Fig. 3(b)] caused a decrease in noise and an increase in selectivity to a region 0.45 mm below the surface. Relative sensitivity to superficial regions decreased while sensitivity to the illumination-collection cone overlap zone seen in Fig. 1(e) increased. However, the higher sensitivity region is oval
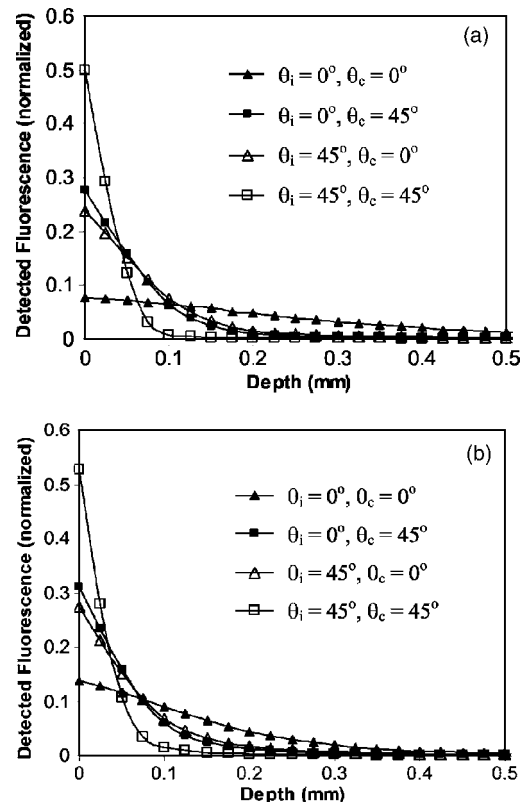

Fig. 2 Depth-resolved graphs of the effect of illumination and collection angle on relative sensitivity for overlapping spot designs. Graphs present data for (a) low and (b) high attenuation cases. Label for each curve indicates type of illumination and collection geometry, respectively. Data have been normalized to total detected signal.
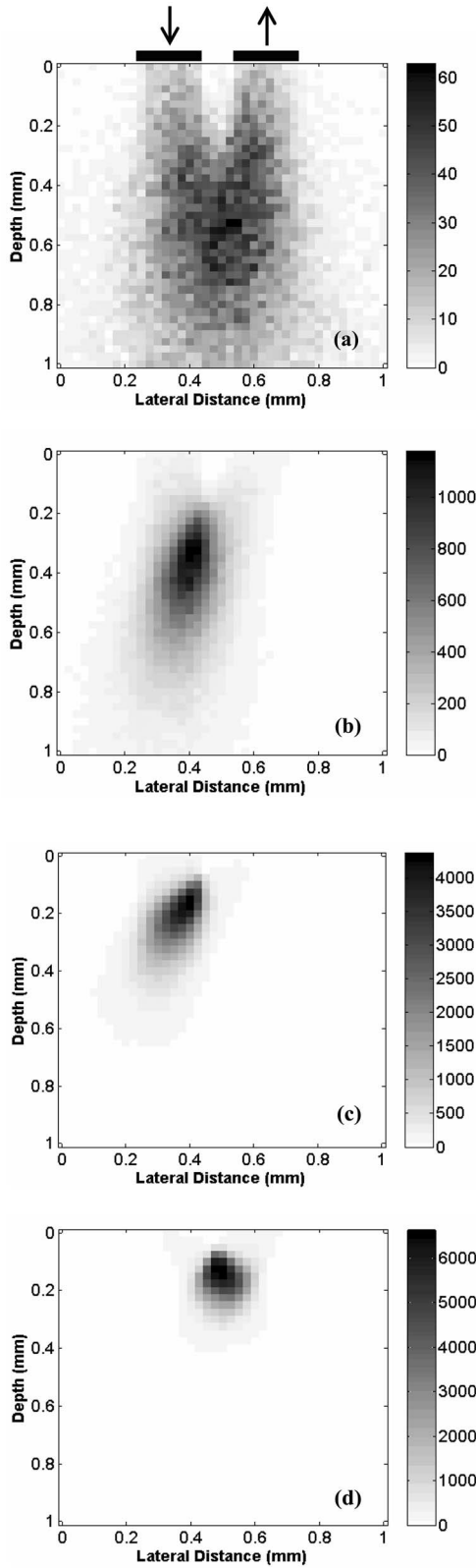
Fig. 3 Contour plots of the effect of illumination and collection angle on signal origin for the low attenuation case, where $L=0.1$ mm. The illumination-collection geometries shown are: (a) $\theta_i=0$ deg, $\theta_c=0$ deg; (b) $\theta_i=0$ deg, $\theta_c=22$ deg; (c) $\theta_i=0$ deg, $\theta_c=45$ deg; and (d) $\theta_i=45$ deg, $\theta_c=45$ deg. Scale represents the number of emission photons detected from each bin location. In all cases, the illumination fiber is on the left side.
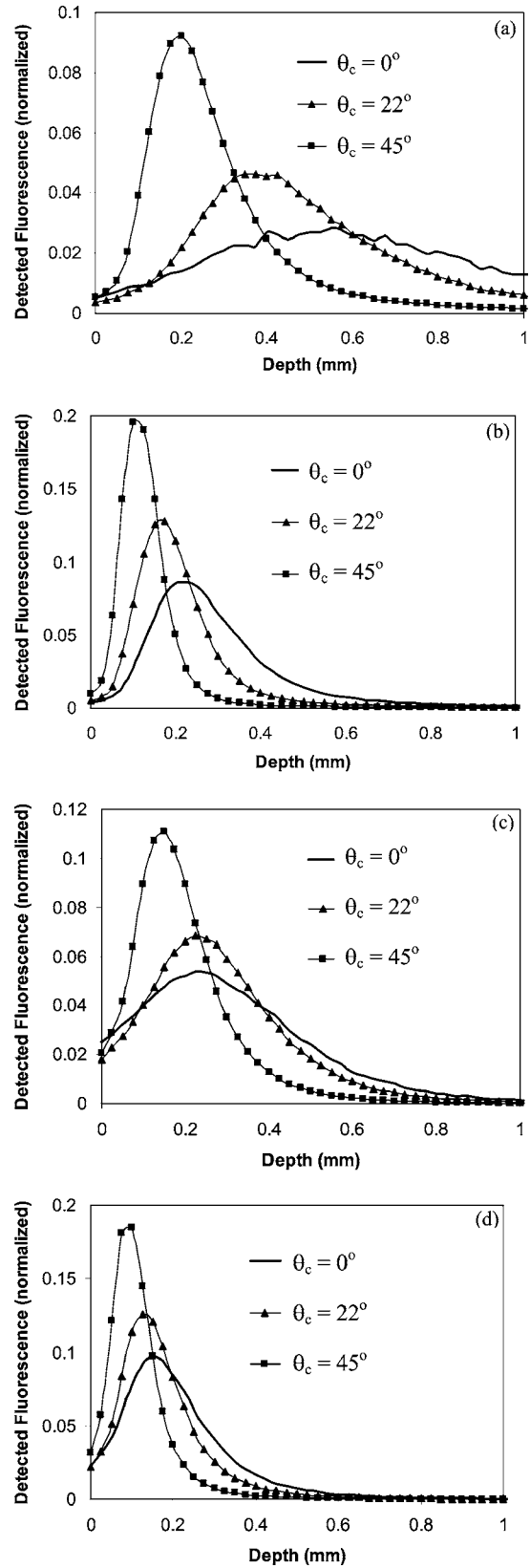

Fig. 4 Effect of illumination and collection angle for nonoverlapping geometries where $L=0.1$ mm. The four graphs represent two optical property sets and two illumination geometries: (a) low attenuation, $\theta_i=0$ deg; (b) low attenuation, $\theta_i=45$ deg; (c) high attenuation, $\theta_i=0$ deg; and (d) high attenuation, $\theta_i=45$ deg. For each graph, three collection angles are presented as specified.
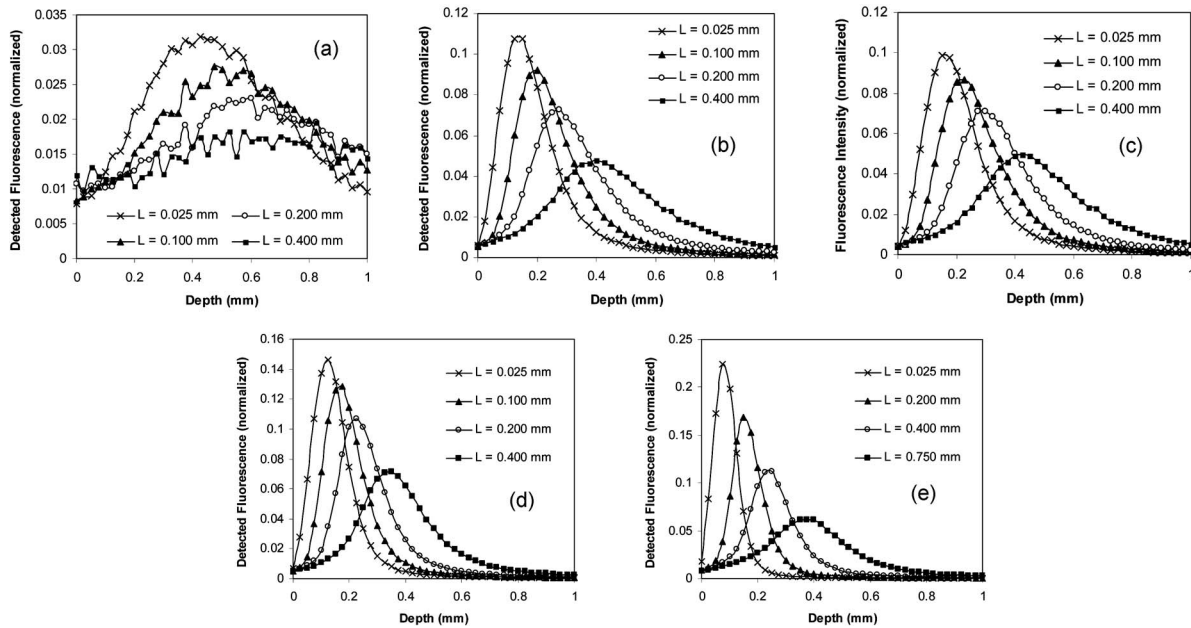
Fig. 5 Effect of spot separation distance (L) for the low attenuation case. The five graphs represent different illumination-collection geometries: (a) $\theta_i = 0$ deg, $\theta_c = 0$ deg; (b) $\theta_i = 0$ deg, $\theta_c = 45$ deg; (c) $\theta_i = 45$ deg, $\theta_c = 0$ deg; (d) $\theta_i = 45$ deg, $\theta_c = 22$ deg; and (e) $\theta_i = 45$ deg, $\theta_c = 45$ deg. Note that a different set of separation distances were used in (e).
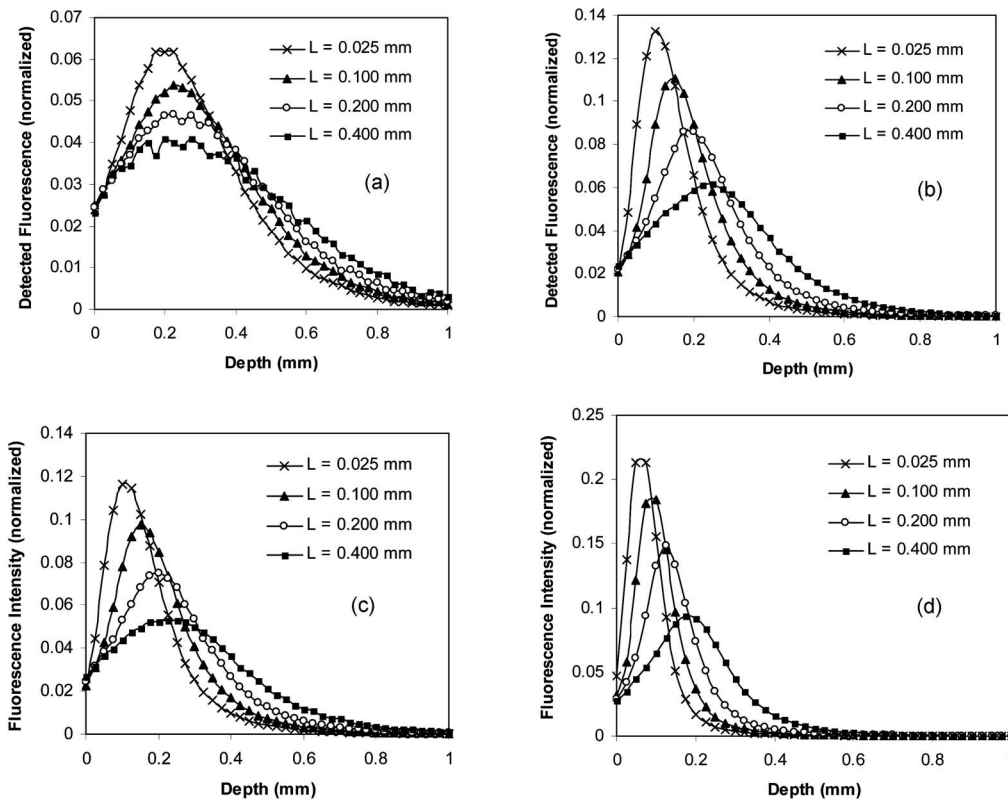
Fig. 6 Effect of illumination-collection spot separation distance (L) for the high attenuation case. The four graphs represent four cases: (a) $\theta_i = 0$ deg and $\theta_c = 0$ deg; (b) $\theta_i = 0$ deg and $\theta_c = 45$ deg; (c) $\theta_i = 45$ deg and $\theta_c = 0$ deg; and (d) $\theta_i = 45$ deg and $\theta_c = 45$ deg.
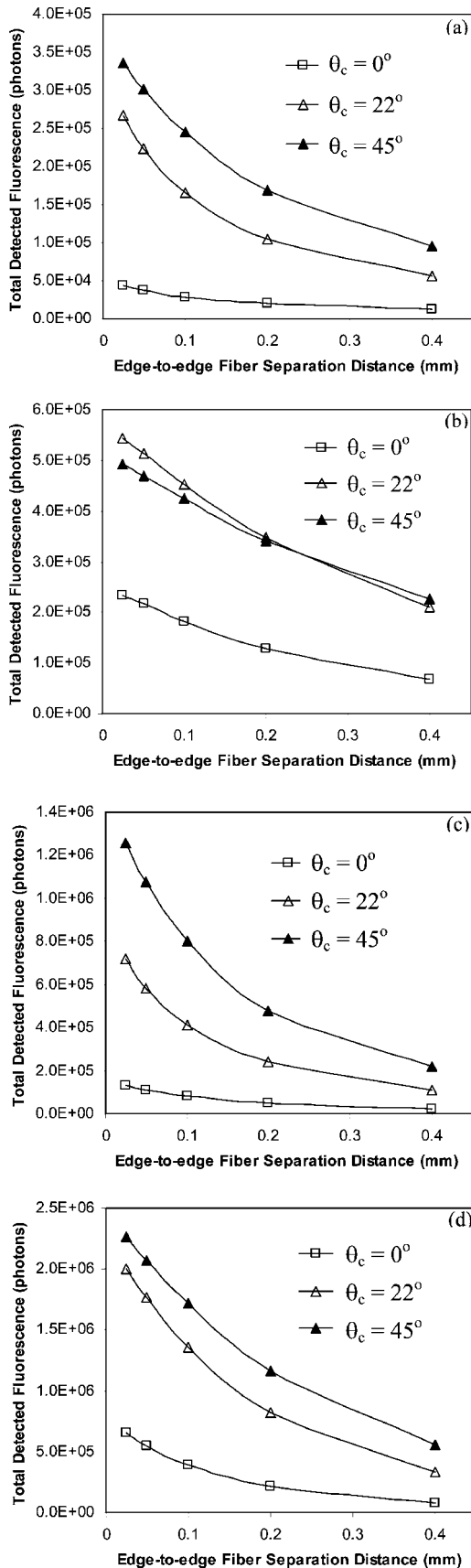
Fig. 7 Detected signal intensity as a function of probe design for (a) low attenuation $\theta_i=0$ deg, (b) low attenuation, $\theta_i=45$ deg, (c) high attenuation, $\theta_i=0$ deg, and (d) high attenuation $\theta_i=45$ deg.

shaped, likely due to light scattering. For a $\theta_c=45$ deg design [Fig. 3(c)], the location of greatest sensitivity was located about 0.2 mm below the surface and had sharper boundaries that were almost triangular, corresponding to the superficial edge of the overlap region. In both Figs. 3(b) and 3(c), the high-sensitivity region was almost directly below the illumination spot. When θ_i was increased to 45 deg [Fig. 3(d)], the high-sensitivity region moved to a location approximately halfway between the illumination and collection spots, as expected from Fig. 1(e). This change also caused an increase in selectivity, with very high sensitivity occurring in a circular region about 0.2 mm in diameter. While the location of this region is expected, the apparently circular shape is not, although this region is so small that its edges are distorted due to the size of the bins. The difference in signal intensity between these plots is an indication of the large changes in sensitivity that can occur as a result of device design.

1-D graphs of fluorescence signal origin for separated spot geometries are presented in Fig. 4. These data document the influence of illumination and collection angle as well as attenuation level. Changes in θ_i or θ_c had very similar affects, with increasing angles resulting in greater selectivity and a reduction in peak sensitivity depth. For example, the depth of the sensitivity peaks in Fig. 4(a) changed from 0.375 mm at $\theta_c=22$ deg to 0.2 mm at $\theta_c=45$ deg, while the corresponding full-width at half-maximum (FWHM) decreased from 0.425 to 0.225 mm. Exceptions to this trend were seen for high attenuation cases in Figs. 4(c) and 4(d), where shift in peak location was minimal as θ_c increases. It is also worth noting that minimal signal was detected from depths below 0.5 mm for the high attenuation cases, which may indicate the limit of probing depth for this technique, whereas significant signal can be obtained for the low attenuation case up to about 0.8 mm below the surface.

High attenuation results tended to produce sensitivity peaks that were greater and more superficial than their low attenuation counterparts, particularly for smaller angle geometries. Additionally, the widths of these peaks decreased with attenuation, for example, a change in FWHM peak width from 0.425 to 0.325 mm was produced for the $\theta_i=0$ deg, $\theta_c=22$ deg geometry. These changes were likely due to the reduction in photon penetration depth produced by the high attenuation case. However, the effect of attenuation on signal origin was reduced as θ_i or θ_c increased, to the point where for the $\theta_i=45$ deg, $\theta_c=45$ deg geometry, the peak height, width, and depth were very similar for both attenuation cases. This is likely a result of high angle geometries detecting excitation-emission photon pairs with shorter path lengths, therefore making these designs less susceptible to absorption-related effects.

The effect of L on signal origin is shown for low and high attenuation cases in Figs. 5 and 6, respectively. These figures contain graphs representing different combinations of θ_i and θ_c. The greatest variations in signal origin distributions are produced for the low attenuation cases in Fig. 5. The normal-incidence case is represented in Fig. 5(a), and indicates a very homogeneous signal origin (and low signal level, which causes the high level of variability). As θ_i or θ_c are increased, the distributions become more selective to specific depth ranges; however, for each combination of angles, the separa-

tion distance has a strong effect on the location and selectivity of interrogation. Increasing separation distance caused increases in peak depth and width. For example, in Fig. 5(c), as L increased from 0.025 to 0.4 mm, the peak sensitivity depth increased from 0.15 to 0.425, and the FWHM increased from 0.2 to 0.375. The separation distances in Fig. 5(e) are different than those in the remainder of Fig. 5 to investigate the potential for achieving high selectivity at greater depths. For the largest L values investigated in Figs. 5(c)–5(e) the peak sensitivity depths were 0.425, 0.35, and 0.375, and the FWHM values were 0.375, 0.275, and 0.3, respectively. These values indicate that the tradeoff between depth of peak sensitivity and selectivity can be modified using θ_i, θ_c, or L; however, several combinations of these parameters can be used to achieve relatively high selectivity at moderate depths. This tradeoff in depth of peak versus selectivity is likely a result of beam divergence due to the illumination and collection cones as well as scattering.

The high attenuation results in Fig. 6 show sensitivity peaks that are more superficial than in Fig. 5. For example, the $L=0.4$ mm case for $\theta_i=45$ deg, $\theta_c=45$ deg has a maximum sensitivity depth of 0.175 mm, as opposed to the 0.225-mm value for the corresponding geometry in Fig. 5(e). Additionally, the larger separation distance curves in Fig. 6 tend to show a rounded peak, possibly due to the higher level of scattering. These differences are most noticeable for larger L values, and appear to decrease with L. The sensitivity to deeper regions is minimal for the high attenuation case, indicating the difficulty of interrogating deep fluorophores. In general, the graphs in Fig. 6 show several common effects, including a shift in the location of subsurface peaks toward greater depths as L is increased, although this effect is less than that seen for the low attenuation case, and quite minimal for the $\theta_i=0$ deg case. Maximum sensitivity (peak height) showed a significant decrease with L. Direct comparison between Figs. 6(b) and 6(c) indicate minimal differences, with the oblique-incidence collection case [Fig. 6(b)] providing slightly greater selectivity.

Detected fluorescence signal intensity data is presented in Fig. 7. These graphs contain data for the low attenuation [Figs. 7(a) and 7(b)] and high attenuation [Figs. 7(c) and 7(d)] cases and either $\theta_i=0$ deg [Figs. 7(a) and 7(c)] or $\theta_i=45$ deg [Figs. 7(b) and 7(d)]. Detected signal intensity decreased exponentially with illumination-collection spot separation distance (R^2 values for these fits ranged from 0.97 to 0.99). While this relationship is similar to that found for normal-incidence probes in our prior study,[4] simulation data from Skala et al.[13] appear to indicate an approximately linear relationship between separation distance and detected signal when $\theta_i=45$ deg and $\theta_c=0$ deg, but an approximately exponential relationship for $\theta_i=0$ deg and $\theta_c=0$ deg, although no fitting data were provided. The source of this discrepancy is not known.

In general, increased illumination/detection angle caused an increase in detected signal. It is likely that this is due to the fact that larger angles reduce the depth of the subsurface overlap region. As a result, the average excitation-emission pathlength decreases as does the level of light absorption. The few exceptions to this trend occurred for the high attenuation/angled illumination case [Fig. 7(b)] as the θ_c was changed

from 22 to 45 deg. The near equivalence in detected signal level for these two cases is likely due to the fact that the overlap regions for these two cases become similar as θ_c increases and L decreases. One possible reason for the higher signal at $\theta_c=45$ and small L values is that there is a smaller field of view represented by the 45 deg case based on the overlap area as opposed to that of the 22 deg case.

4 Discussion

Depth-dependent variations in sensitivity to tissue fluorophores are strongly influenced by device-tissue interface parameters. By exploiting known variations, it may be possible to selectively interrogate individual tissue layers or determine the optical characteristics of tissue as a function of depth. Such abilities are particularly interesting in light of studies that indicate that disease progression can cause changes in the endogenous fluorescence characteristics and morphology of individual tissue layers.[8,9,15] For example, fluorescence originating from the epithelial layer of cervical tissue has been shown to increase with neoplastic progression. This layer is on the order of 350 μm thick and contains three primary fluorophores—tryptophan, NADH, and FAD—of which the latter two are mitochondrial components. Fluorescence generated in the deeper stromal layer is primarily due to collagen and has been shown to decrease with disease onset. While the sensitivity distributions of normal-incidence designs have been investigated, it is likely that angled delivery and collection may enable further improvements in selective interrogation of tissue layers, such as the epithelium and stroma of cervical tissue. The unique insights provided by this study should improve understanding of basic light-tissue interaction effects, as well as provide insights on device design that are relevant to cervical cancer detection and a range of other public health issues.

4.1 Basic Trends in Signal Origin

The basis for achieving selectivity using oblique-incidence geometries—the intersection of illumination and collection cones within the tissue—is extremely simple. However, the question of predicting depth-resolved signal origin rapidly becomes quite complex due to the numerous variables involved in device-tissue interface design and optical properties. Changes in θ_i or θ_c produced some of the most significant variations in signal origin distributions. For both overlapping and separated spot geometries, increasing these angles caused a dramatic increase in spatial selectivity. In prior studies, geometries with small, overlapping illumination and collection spots have shown a high degree of selectivity for superficial regions. This selectivity became even greater as θ_i or θ_c increased, with changes in θ_c producing a slightly stronger effect than θ_i. Relative sensitivity to fluorophores in the most superficial 50 μm increased by 3 to 4 times as illumination and detection angles were increased. It is likely that this is due to the elimination of illumination-detection cone overlap in deeper regions (Fig. 1), which makes it unlikely that photons emitted at deeper locations will be detected.

In comparison to normal-incidence designs, angled geometries produce more selective interrogation of subsurface locations, due at least in part to a reduction in sensitivity to regions that are deeper than the peak sensitivity depth. For

nonoverlapping spot designs, increasing θ_i or θ_c caused a decrease in both the depth of peak sensitivity and the width of this peak (the extent of the region most strongly interrogated). Both of these trends agree with the illustrations in Fig. 1. To counteract the decrease in peak sensitivity depth with θ_i and θ_c, spot separation distance can be increased. However, the high degree of selectivity produced for short separation distances is reduced as separation increases, most likely due to an increase in scattering events with path length. The deepest sensitivity peaks produced by angled designs for the low attenuation case were 0.4 to 0.5 mm below the surface and generated 3 to 5 times greater sensitivity at this depth than in regions 0.2 mm or more from the peak. For the high attenuation case, angled designs generated moderately high selectivity to superficial, subsurface regions (e.g., 0.1- to 0.2-mm depths). However, collecting significant fluorescence from deeper locations or rejecting signals originating from very superficial regions was not possible to any great extent for this optical property set. These results indicate the potential depth limits on subsurface selectivity for highly attenuating turbid media.

The two sets of optical properties investigated in this study provide essential insights into the behavior of angled illumination-collection geometries in different situations. For separated spot designs, an increase in attenuation tended to cause a decrease in probing depth and increase in selectivity (higher sensitivity peak and reduced sensitivity to deeper regions). Changes in signal origin with optical property were not as significant for overlapping spot designs, likely because the average path length for these probes is smaller, thus minimizing the effect of absorption. The changes caused by optical property variation for separated spot geometries appear to indicate that these designs are more effective for cases in which attenuation is reduced, such as at longer wavelengths. This is not an unexpected result, as the simple light propagation pathways illustrated in Fig. 1 would become increasingly distorted as scattering and absorption levels increased. The effect of optical properties is a complex one that cannot be thoroughly elucidated using two sets of optical properties. Due to the fact that every simulation requires a set of absorption and scattering coefficients for the excitation and emission light propagation computations, a large number of individual simulations may be needed to characterize the specific changes induced by optical property variations.

4.2 Light Propagation Mechanisms

The primary mechanisms that make angled geometries superior to their normal-incidence counterparts are not well understood. A prior study concluded that oblique incidence probes cause excitation photons and emission photons to travel a shorter path length before they reach the collection fiber, thus increasing the sensitivity to superficial regions.[13] Our results indicate that detected signal origin is strongly influenced by two factors: the overlap of illumination and collection cones and tissue optical properties. To understand the role of interface design, it is useful to start with a low attenuation case. When μ_s' is low and the probability of a photon deviating significantly from a linear path is small, fluorescence will typically only be detected if the excitation photon is absorbed in the cone overlap volume and fluorescence emitted in the

direction of the detector. If emission takes place outside of the overlap region (or in a direction away from the detector), detection requires the trajectory of the excitation and/or emission photon to be altered, which is unlikely. Oblique incidence designs [eg., Figs. 1(e) and 3(b)] have cone overlap regions that are limited to a relatively small range of depths, and are thus able to target well-defined regions. Normal-incidence geometries [e.g., Figs. 1(d) and 3(a)], however, depend on cone overlap regions that are not restricted in depth or detection of fluorescence from nonoverlap regions. Therefore, both selectivity and signal intensity for the latter approach is inherently limited.

Light propagation mechanisms become more complicated as attenuation increases. Higher μ_a levels induce stronger decays in photon absorption with depth, making it more difficult to detect fluorescence from deeper regions. Thus, signal origin distributions are shifted toward the surface, out of the cone overlap region. As μ_s' increases, the probability of large deviations in photon trajectory increases, light propagation becomes more diffuse, and the number of photons detected from outside the overlap region increases. As a result, the ability to target a specific region is reduced, the cone overlap approach becomes less effective in approximating signal origin, and the advantage of an angled approach is reduced.

4.3 Optimization of Device-Tissue Interface Design

One of the considerations in optimizing probe design using angled fiber probes is whether one or both fibers should be angled. Prior studies have shown that overlapping spot geometries tend to produce greater sensitivity to highly superficial fluorophores as compared to nonoverlapping designs. An overlapping spot design that incorporates angled illumination or collection can increase the selectivity to highly superficial regions, and if both channels are angled, the probed region is further limited. However, the nonoverlapping spot case is not as clearly defined. If θ_i or θ_c are increased to improve selectivity, then the depth of peak sensitivity is reduced. If spot separation distance is then increased to achieve the original depth of peak sensitivity, the level of selectivity decreases to a level that does not appear to be much superior to that obtained using the original angle.

A prior study involved the use of an angled illumination fiber and a normal-incidence collection fiber.[13] Our simulations indicate that the opposite configuration—a normal-incidence fiber for illumination and one or more angled fibers for collection—provides similar signal origin distributions. However, Figs. 7(a) and 7(b) indicate that the intensity of the detected signal for $\theta_i=45$ deg, $\theta_c=0$ deg is less than for $\theta_i=0$ deg, $\theta_c=45$ deg, independent of separation distance. This is likely due to the fact that for the $\theta_i=45$ deg case, excitation light has to travel a greater distance to reach the overlap region than in the normal illumination case. Since the absorption coefficient is higher for excitation light than emitted light, the extra distance traveled results in greater attenuation. In other words, to maximize detected fluorescence signal, a device should be designed to minimize the length of the excitation path as opposed to the emission path. Detected signals can also be maximized by increasing the collection efficiency of the interface geometry. While the collection efficiency of a probe with normal-incidence illumination can be improved by

placing multiple fibers in a concentric ring around the illumination fiber, such an approach would not be appropriate for an angled illumination fiber given the lack of symmetry. Placing a ring of angled illumination fibers around a single normal-incidence collection fiber will not improve signal detection, given that the same energy is delivered (which may be limited by safety considerations).

In addition to elucidating light-tissue interactions during fluorescence spectroscopy, this study provides further evidence of the utility of Monte Carlo modeling. This well-established approach provides a simple way to estimate the influence of changes in a variety of device and/or tissue parameters. Although processing time can become a limiting factor for low collection efficiency cases such as those in this study, it is possible to offset this inefficiency by collecting data for multiple interface geometries in a single simulation. One of the primary benefits of this technique is that it facilitates the study of a wide parameter space so as to provide a thorough characterization. Furthermore, variables such as signal origin distributions are much easier to generate using a model than under experimental conditions. While additional modeling studies involving single-layer geometries are warranted to investigate basic issues, application-oriented research will require the investigation of cases with more realistic tissue morphology, such as multilayer models.[6,13,16] More realistic representation of devices, such as fiber optic probes will also be needed to improve the accuracy and realism of future simulations. Models that can incorporate these advances while providing flexibility will be powerful tools for both *a priori* design and the optimization of existing optical diagnostic devices for a wide variety of medical applications.

Although this study represents a large step toward understanding the performance of oblique-incidence geometries, the issues that remain unresolved are as numerous as the myriad of fiber optic devices that have[2] and will be developed. In the future, it will be useful to address the effect of numerical aperture, fiber diameter, beam shape, angular launch distribution, absorption, scattering and anisotropy coefficients at excitation and emission wavelengths, as well as optical property and morphological variations in layered tissue.

Acknowledgments

References

1. G. A. Wagnieres, W. M. Star, and B. C. Wilson, "*In vivo* fluorescence spectroscopy and imaging for oncological applications," *Photochem. Photobiol.* **68**, 603–632 (1998).
2. U. Utzinger and R. R. Richards-Kortum, "Fiber optic probes for biomedical optical spectroscopy," *J. Biomed. Opt.* **8**(1), 121–147 (2003).
3. T. J. Pfefer, K. T. Schomacker, M. N. Ediger, and N. S. Nishioka, "Light propagation in tissue during fluorescence spectroscopy with single-fiber probes," *IEEE J. Sel. Top. Quantum Electron.* **7**, 1004–1012 (2001).
4. T. J. Pfefer, K. T. Schomacker, M. N. Ediger, and N. S. Nishioka, "Multiple-fiber probe design for fluorescence spectroscopy in tissue," *Appl. Opt.* **41**, 4712–4721 (2002).
5. T. J. Pfefer, L. S. Matchette, A. M. Ross, and M. N. Ediger, "Selective detection of fluorophore layers in turbid media: the role of fiberoptic probe design," *Opt. Lett.* **28**, 120–122 (2003).
6. C. Zhu, Q. Liu, and N. Ramanujam, "Effect of fiber optic probe geometry on depth-resolved fluorescence measurements from epithelial tissues: a Monte Carlo simulation," *J. Biomed. Opt.* **8**(2), 237–247 (2003).
7. L. Quan and N. Ramanujam, "Relationship between depth of a target in a turbid medium and fluorescence measured by a variable-aperture method," *Opt. Lett.* **27**, 104–106 (2002).
8. R. Drezek, K. Sokolov, U. Utzinger, I. Boiko, A. Malpica, M. Follen, and R. Richards-Kortum, "Understanding the contributions of NADH and collagen to cervical tissue fluorescence spectra: Modeling, measurements, and implications," *J. Biomed. Opt.* **6**(4), 385–396 (2001).
9. G. I. Zonios, R. M. Cothren, J. T. Arendt, J. Wu, J. Van Dam, J. M. Crawford, R. Manoharan, and M. S. Feld, "Morphological model of human colon tissue fluorescence," *IEEE Trans. Biomed. Eng.* **43**, 113–122 (1996).
10. T. F. Cooney, H. T. Skinner, and S. M. Angel, "Comparative study of some fiber-optic remote Raman probe designs. Part I: Model for liquids and transparent solids," *Appl. Spectrosc.* **50**, 836–848 (1996).
11. T. F. Cooney, H. T. Skinner, and S. M. Angel, "Comparative study of some fiber-optic remote Raman probe designs. Part II: Tests of some single-fiber, lensed, and flat-and bevel-tip multi-fiber probes," *Appl. Spectrosc.* **50**, 849–860 (1996).
12. M. G. Shim, B. C. Wilson, E. Marple, and M. Wach, "Study of fiber-optic probes for *in vivo* medical Raman spectroscopy," *Appl. Spectrosc.* **53**, 619–627 (1999).
13. M. C. Skala, G. M. Palmer, C. Zhu, Q. Liu, K. M. Vrotsos, C. L. Marshek-Stone, A. Gendron-Fitzpatrick, and N. Ramanujam, "Investigation of fiber-optic probe designs for optical spectroscopic diagnosis of epithelial pre-cancers," *Lasers Surg. Med.* **34**, 25–38 (2004).
14. L. Nieman, A. Myakov, J. Aaron, and K. Sokolov, "Optical sectioning using a fiber probe with an angled illumination-collection geometry: evaluation in engineered tissue phantoms," *Appl. Opt.* **20**, 1308–1319 (2004).
15. K. T. Schomacker, J. K. Frisoli, C. C. Compton, T. J. Flotte, J. M. Richter, N. S. Nishioka, and T. F. Deutsch, "Ultraviolet laser-induced fluorescence of colonic tissue: basic biology and diagnostic potential," *Lasers Surg. Med.* **12**, 63–78 (1992).
16. T. J. Pfefer, L. S. Matchette, and R. A. Drezek, "Influence of illumination-collection geometry on fluorescence spectroscopy in multi-layer tissue," *Med. Biol. Eng. Comput.* **42**, 669–673 (2004).